Inorganic Chemistry

pubs.acs.org/IC Article

Polymorphs of Rb_3ScF_6: X-ray and Neutron Diffraction, Solid-State NMR, and Density Functional Theory Calculations Study

Aydar Rakhmatullin,* Maxim S. Molokeev, Graham King, Ilya B. Polovov, Konstantin V. Maksimtsev, Erwan Chesneau, Emmanuelle Suard, Rinat Bakirov, František Šimko, Catherine Bessada, and Mathieu Allix

Cite This: *Inorg. Chem.* 2021, 60, 6016–6026 Read Online

ACCESS | Metrics & More | Article Recommendations | Supporting Information

ABSTRACT: The crystal structures of three polymorphs of Rb_3ScF_6 have been determined through a combination of synchrotron, laboratory X-ray, and neutron powder diffraction, electron diffraction, and multinuclear high-field solid-state NMR studies. The room temperature (RT; α) and medium-temperature (β) structures are tetragonal, with space groups $I4_1/a$ (Z = 80) and $I4/m$ (Z = 10) and lattice parameters a = 20.2561(4) Å, c = 36.5160(0) Å and a = 14.4093(2) Å, c = 9.2015(1) Å at RT and 187 °C, respectively. The high-temperature (γ) structure is cubic space group $Fm\bar{3}m$ (Z = 4) with a = 9.1944(1) Å at 250 °C. The temperatures of the phase transitions were measured at 141 and 201 °C. The three α, β, and γ Rb_3ScF_6 phases are isostructural with the α, β, and δ forms of the potassium cryolite. Detailed structural characterizations were performed by density functional theory as well as NMR. In the case of the β polymorph, the dynamic rotations of the ScF_6 octahedra of both Sc crystallographic sites have been detailed.

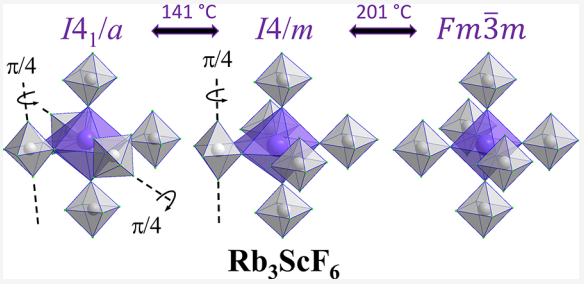

INTRODUCTION

Alkali-metal fluoroscandates have recently attracted much attention because of their promising potential use in many areas such as fluorescent probes, solar cell, solid-state lasers, and other fields.[1−7] Because of their specific electronic configurations and the small ionic radius of scandium compared to other rare-earth elements, fluoroscandates doped with Mn^{4+} or Ln^{3+} can generate interesting optical properties, as was recently demonstrated for $NaScF_4$,[3,4] KSc_2F_7,[5,8] and K_3ScF_6.[9] Mn^{4+}-doped K_3AlF_6 has been latterly reported to show high color-rendering properties.[10] As demonstrated below, Rb_3ScF_6 is isostructural with K_3AlF_6.[1,2] The specific crystal symmetry of the polymorphs, phase transitions, and associated physical properties of the studied compound may be related to the structural particularities of this class of compounds, which is named halide double perovskites ($A_2BB'X_6$). The double perovskite structure is so-called because the unit cell of a double perovskite is twice as large as that of a simple ABX_3 perovskite. Moreover, K_3AlF_6 exhibits superstructure polymorphs, which was attributed to the noncooperative octahedral tilting (NCOT).[1,2] Such structures are highly complex and difficult to study. Additionally, the dynamic motion of the AlF_6 octahedra in K_3AlF_6 was established. Exact knowledge of the structure and dynamics of these various crystalline materials is required to understand their functionalities and to further improve their properties to suit the above-mentioned applications.

Structural studies on almost all reported lithium, potassium, and sodium fluoroscandates have been performed. Recently, the structures of two members of the CsF-ScF_3 system, $CsScF_4$ and $CsSc_3F_{10}$, have been reported.[11,12] However, rubidium-containing fluoride compounds have been overlooked. Only the structure of the RT $RbSc_3F_{10}$ polymorph has been reported to date. It is worth noting that this study was only published in a Ph.D. manuscript and is not included in structural databases.[13] Regarding Rb_3ScF_6, Turrell et al.[14] found that the compound undergoes two polymorphic transformations at 154 and 200 °C. From X-ray powder diffraction data, it was proposed that the room temperature (RT) and medium-temperature structures are tetragonal, with space group $P4/mnc$ (Z = 128) at RT and the lattice parameters a = 6.419 Å, c = 9.154 Å and a = 6.467 Å, c = 9.222 Å at RT and 177 °C, respectively. The high-temperature (HT) structure was reported to be cubic space group $Fm\bar{3}m$ (Z = 4) with a = 9.214 Å at 250 °C. From variable-temperature Raman spectroscopy experiments, the authors stated that all polymorphs contain isolated ScF_6^{3-} octahedra. However, only cell parameters and space groups were proposed for the

Received: February 18, 2021
Published: April 7, 2021

https://doi.org/10.1021/acs.inorgchem.1c00485
Inorg. Chem. 2021, 60, 6016–6026

three polymorphs, and the crystalline structures have not been established.

In this paper, we used a combined approach including solid-state NMR spectroscopy, transmission electron microscopy, and synchrotron and neutron powder diffraction to precisely determine the structure of three Rb_3ScF_6 polymorphs between RT and HT. In addition, we employed in situ HT magic-angle-spinning (MAS) NMR experiments to follow the structural transitions and dynamics. 2D multiquantum MAS (MQMAS) NMR methods enabled one to enhance the spectral resolution by spreading signals in two spectral dimensions. HT MAS NMR is an unusual method for structural characterization. Here, we show that the use of this technique can provide an accurate description of the phase transitions, as well as quantitative and qualitative information on the structure and dynamics.

EXPERIMENTAL SECTION

Synthesis. Rubidium fluoride (Aldrich, 99.8%) and scandium fluoride (JSC Dalur, >99%) powder precursors were used for the synthesis of Rb_3ScF_6. The salts were first dried under vacuum at 150 °C for 6 h and then transferred to an argon-filled glovebox. All of the manipulations were performed in an argon-filled glovebox, unless mentioned otherwise. Both salts were then mixed and homogenized in an agate mortar in the required proportions (5 g of the mixture; 3.7727 g of RbF and 1.2273 g of ScF_3) and placed in a nickel crucible covered with a nickel lid. The synthesis was performed by a solid-state reaction inside the glovebox to exclude possible contamination by moisture and minimize the influence of oxygen. The crucibles were placed in the furnace, and the heating was performed at 840 °C for 6 h with a heating rate of 5 °C min^{-1}. The furnace was then cooled with a rate of 2 °C min^{-1}, and the crucibles were taken out and weighed. The changes of the crucible's mass did not exceed 10 mg, and vapor deposition was not noticed. The resulting pale-white salt was extracted from the crucible outside the glovebox and homogenized.

Thermal Analysis Measurements. Differential scanning calorimetry (DSC) was used for following the phase transformations taking place during both heating and cooling of Rb_3ScF_6. The measurements were performed with a Mettler Toledo STAR DSC823 calorimeter equipped with a FRS 5 sensor and 56 Au−Au/Pd thermocouples (a working range of 10−700 °C and a resolution of <0.04 μW). The Rb_3ScF_6 samples were loaded in a platinum crucible and heated from 25 to 260 °C at 5 °C min^{-1} (heating) and 7 °C min^{-1} (cooling). A dry air flow through the furnace was maintained at a 50 mL s^{-1} rate.

Electron Diffraction. Selected-area electron diffraction (SAED) patterns were collected on a Philips CM20 transmission electron microscope fitted with an Oxford energy-dispersive spectrometry (EDS) analyzer. The sample was first crushed in ethanol, and then a drop of the solution with the small crystallites in suspension was deposited onto a carbon-coated copper grid.

X-ray Powder Diffraction. High-resolution synchrotron powder diffraction data were collected at the 11-BM beamline at the Advanced Photon Source, Argonne National Laboratory, using a wavelength of 0.457893 Å at RT and 0.457901 Å at 187 °C. The powder was packed into a kapton capillary with an outer diameter of 0.8 mm and spun during data acquisition from 0.5 to 50° (2θ) using 0.001° steps.

HT X-ray powder diffraction data were recorded on a Bragg−Brentano D8 Advance Bruker diffractometer (Cu Kα radiation) equipped with a LynxEye XE detector over an angular range of 5° < 2θ < 130°.

Rietveld refinements were performed using the *Topas 4.2*[15] and *JANA2006*[16] software.

Neutron Powder Diffraction. Neutron powder diffraction data were obtained at the Institute Laue Langevin (Grenoble, France) on the D2B diffractometer at RT using an 8-mm-diameter vanadium tube. Data were collected with a wavelength of 1.59354 Å over a range of 0° < 2θ < 160° with a 0.05° step size.

NMR Spectroscopy. RT solid-state MAS NMR spectra were recorded on Bruker Avance III HD 17.6 and Avance NEO 20 T spectrometers using 1.3 and 2.5 mm resonance probes at a MAS frequency of 60 or 30 kHz, respectively. The ^{19}F, ^{45}Sc, and ^{87}Rb radio-frequency (RF) strengths were 190, 464, and 83 kHz, respectively. ^{87}Rb MQMAS NMR spectra were acquired in two different ways, i.e., by Z-filtering[17] and using the RIACT excitation method.[18] The Z-filter experiment parameters were identical with those used in our previous study.[19] RIACT MQMAS NMR spectra were measured using the two-pulse RIACT (II) sequence[20] with pulse widths of 3.7 and 8 μs, at a RF field of ∼150 kHz. The sweep widths were 500 and 120 kHz ($4\nu_r$) in the direct and indirect dimensions. A recycle delay of 0.1 s was used.

HT data were collected at 17.6 T using a MAS LASER probe with boron nitride crucibles contained in a 7 mm zirconia bottom-less rotor spinning at 6 kHz. The diode laser beam (DILAS, 200 W, 980 nm) is guided by fiber optics to the crucible. Unfortunately, a significant temperature gradient was detected in the sample due to heating of the container from the bottom only. To decrease the temperature gradient inside the sample, only about 20 mg of powder was placed in the crucible.

In order to improve the resolution, two decoupling pulse schemes were applied: continuous wave (10 kHz for ^{19}F and 5 kHz for ^{45}Sc) in the case of HT experiments and PISSARRO[21] ^{45}Sc and ^{19}F in the case of a MAS frequency of 30 or 60 kHz. ^{19}F, ^{45}Sc, and ^{87}Rb chemical shifts are referenced to $CFCl_3$, a 0.11 M $ScCl_3$ solution in 0.05 M HCl, and 0.01 M $RbNO_3$, respectively. The NMR parameters (chemical shifts, line widths, and quadrupolar parameters) were fitted for several different rotation frequencies and for two magnetic fields to the experimental spectra by means of the *DMfit* program.[22] Additionally, the simulations of 1D and 2D ^{87}Rb MQMAS and RIACT NMR spectra were performed using a fNMR package, implementing the method described in ref 23.

DFT Calculations. In the case of DFT calculations using the Perdew−Burke−Ernzerhof (PBE) functional[24] for compounds containing Ca, Sc, and La atoms, there is an overestimation of the hybridization between the 2p anion (oxygen or fluorine) orbitals and the unoccupied $3d^0$ and $4f^0$ orbitals. As a consequence of this overestimation, the covalent character of a bond increases and the agreement between the experimental NMR data and theoretical predictions decreases.[25,26] The DFT+*U* method, in which the artificial energy shift *U* of the $3d^0$ states toward higher energy is inducing a decrease of the bond covalency, is a suitable corrective approach on a practical level.[25,26] The convenient value of *U* of the DFT+*U* method depends on the atomic species and surroundings of the atom. To determine suitable values of *U*, a series of calculations were performed using the *CASTEP* module,[27] implemented in the *Materials Studio 7.0* software package. Different *U* values were used for previously studied fluoroscandates.[12,28] The correlations between the calculated isotropic ^{45}Sc and ^{19}F magnetic shielding constants (σ_{iso}) and experimentally determined isotropic (δ_{iso}) chemical shift values have been plotted and fitted by linear regressions (Figure S1). From these fits, R^2 values were obtained. The coefficient of determination should be close to 1. The relationship between R^2 and *U* perfectly fits with a parabolic curve with maxima at 0.051 and 0.059 hartree for the ^{45}Sc and ^{19}F nuclei, respectively. Consequently, the value *U* = 0.055 hartree was chosen for further calculations (Figure S1).

The cutoff energies were 780 eV, and the *k*-point spacing was 0.04 $Å^{-1}$. The calculations were performed after geometry optimization of all atomic positions, retaining the experimental cell parameters and symmetry constraints. The obtained relationships for ^{45}Sc and ^{19}F at *U* = 0.055 hartree are $\delta_{iso} = -0.8315\sigma_{iso} + 671.7$ and $\delta_{iso} = -0.730\sigma_{iso} + 70.17$, respectively.

RESULTS

The Rb_3ScF_6 material was first checked at RT by X-ray powder diffraction. The data correspond to those reported by Turrell

https://doi.org/10.1021/acs.inorgchem.1c00485
Inorg. Chem. 2021, 60, 6016−6026

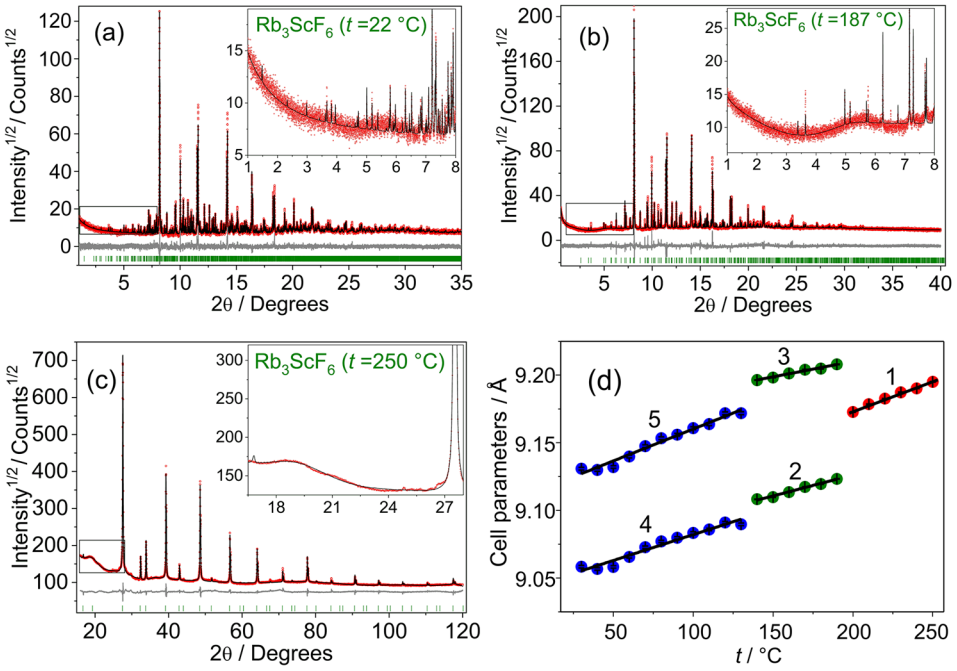

Figure 1. Rietveld refinement of the synchrotron and laboratory X-ray powder diffraction patterns of Rb_3ScF_6 at (a) 22 °C, (b) 187 °C, and (c) 250 °C. Black dots are the observed pattern, red dots are the calculated pattern, vertical green bars are the Bragg positions, and the gray line is the difference between the observed and calculated patterns. (d) Temperature dependence of the unit cell parameters of the α, β, and γ phases: $1 - a$ of the γ phase ($Fm\bar{3}m$), $2 - a/\sqrt{2}.5$ of the β phase ($I4/m$), $3 - c$ of the β phase ($I4/m$), $4 - a/\sqrt{5}$ of the α phase ($I4_1/a$), and $5 - c/4$ of the α phase ($I4_1/a$).

Table 1. Crystallographic Data for the Polymorphs of Rb_3ScF_6 from X-ray Diffraction and Neutron Rietveld Refinement

chemical formula	α-Rb_3ScF_6		β-Rb_3ScF_6	γ-Rb_3ScF_6
source	synchrotron	neutron	synchrotron	laboratory X-ray
fw (g mol^{-1})	415.35		415.35	415.35
temperature (°C)	22	23	187	250
wavelength (Å)	0.457893	1.59354	0.457901	1.5406
cryst syst	tetragonal		tetragonal	cubic
space group	$I4_1/a$ (No. 88)		$I4/m$ (No. 87)	$Fm\bar{3}m$ (No. 225)
unit cell dimens (Å)	a = 20.2561(4)		a = 14.4093(2)	a = 9.1944(1)
	c = 36.5160(0)		c = 9.2015(1)	
cell volume (Å^3)	14982.92(10)		1910.49(7)	777.27(3)
Z	80		10	4
d-space range (Å)	0.67−24.7	0.81−13.0	0.67−24.7	0.89−5.5
2θ range (deg)	5−40	0−160	5−40	16−120
fitting	Rietveld	Rietveld	Rietveld	Rietveld
χ^2	1.49	2.11	2.01	4.01
R_{wp} (%)[a]	13.47	4.70	13.91	3.49
R_p (%)[a]	10.80	3.59	10.64	2.65

[a]For definitions of R factors, see refs 15 and 16.

et al.[14] Then, the phase transitions were analyzed by a DSC method between 25 and 260 °C (Figure S2). The heating curve contains two well-separated peaks at T_{onset} = 137 °C and 200 °C. Both thermal effects represent solid−solid phase transitions characterized by symmetrical endothermic peaks during heating and symmetrical exothermic peaks during cooling. The cooling curve shows that these individual structural modifications are transformed reversibly, at T_{onset} = 202 and 145 °C, respectively. The integral peak area of the thermal effects at cooling is directly proportional to the enthalpy of change during the phase transition. From that, the entropy of change of both transitions are about 0.29 and 0.21 J mol^{-1} K^{-1}, respectively. The measured transition temperatures are slightly different from the previously reported results of Turrell et al. (154 and 200 °C).[14] Hereafter, the three polymorphs are labeled α (RT), β (medium temperature), and γ (HT).

Structure from Powder Diffraction. We first investigated the structure of Rb_3ScF_6 at HT because it corresponds to the highest-symmetry crystal structure. At 250 °C, all X-ray powder diffraction peaks of γ-Rb_3ScF_6 were indexed with a cubic cell ($Fm\bar{3}m$) whose parameter [a = 9.1944(1) Å] is close to that of the δ polymorph of K_3AlF_6.[2] Therefore, this structure (two Rb, one Sc, and one F sites) was used as a starting model for Rietveld refinements (Figure 1c). The K^+ site was replaced by Rb^+ and Al^{3+} by Sc^{3+}, respectively. The thermal parameters

https://doi.org/10.1021/acs.inorgchem.1c00485
Inorg. Chem. 2021, 60, 6016−6026

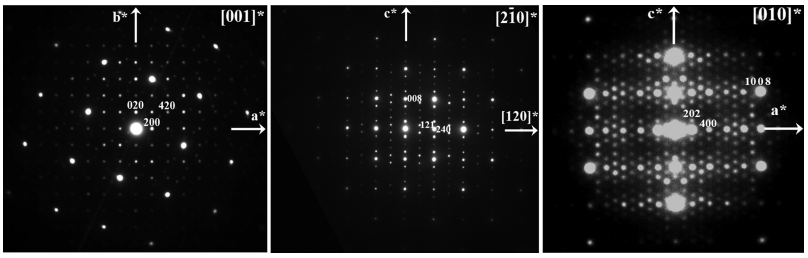

Figure 2. [001]*, [2−10]*, and [010]* SAED patterns of α-Rb_3ScF_6. The indexation corresponds to the a = 20.25 Å and c = 36.5 Å cell with a $I4_1/a$ space group.

of the F crystallographic site were refined anisotropically given the distortion around this anion. Rietveld refinements were stable and led to low R factors (Table 1 and Figure 1c). Atomic coordinates are provided in Table S1, anisotropic thermal parameters (large values, see discussion below) are presented in Table S2, and selected interatomic distances are shown in Table S3.

The powder diffraction pattern corresponding to β-Rb_3ScF_6 and recorded at 187 °C can be indexed with a tetragonal cell ($I4/m$) and cell parameters [a = 14.4093(2) Å and c = 9.2015(1) Å] close to those of β-K_3AlF_6 so that the latter structure was used as a starting model (four Rb, two Sc, and seven F sites).[2] The Rietveld refinement was stable and led to low R factors (Table 1 and Figure 1b), proving that these two phases are isostructural. Coordinates of the atoms and a selection of interatomic distances are shown in Tables S4 and S5.

Both static or dynamic disorder influence the atomic displacement parameter (ADP) values. Previously, large ADP values were observed for K_3AlF_6 and Rb_3AlF_6 and were explained by significant rotations of AlF_6 octahedra.[2,19] As will be shown below from analysis of the HT NMR data, we observe the same dynamic behavior of ScF_6 octahedra, which leads to relatively large ADP values for β and γ polymorphs of Rb_3ScF_6, especially for F atoms.

All synchrotron powder diffraction peaks of α-Rb_3ScF_6 recorded at 22 °C can be indexed with a tetragonal cell ($I4_1/a$) and cell parameters [a = 20.2561(4) Å and c = 36.5160(0) Å], which appears to be isostructural to α-K_3AlF_6.[1] This observation was further confirmed by electron diffraction data, which showed patterns similar to those of α-K_3AlF_6 (Figure 2). Because of the large number of degrees of freedom for the atomic positions (>150), a joint synchrotron and neutron refinement was used to determine the structure of the α phase. The structure of α-K_3AlF_6 was used as a starting model. During the initial steps, all sites corresponding to the same element were constrained to have the same displacement parameter, and soft distance constraints were used for the Sc−F bond length. For the final refinement, the distance constraints could be removed, and each metal site was allowed its own isotropic displacement parameter, while all F sites were constrained to have the same displacement parameter. Fourier difference maps did not show any residue in the background. The fits of the combined Rietveld refinement are shown in Figures 1a and S3. The atomic coordinates, thermal parameters, and Sc−F and Rb−F interatomic distances are gathered in Tables S6 and S7. It should also be noted that it might not be possible to synthesize good-quality single crystals of Rb_3ScF_6 for precise structural elucidation because of the inevitable crystal twinning taking place during cooling in the synthesis process.[29]

An additional 23 laboratory X-ray powder diffraction patterns measured at different temperatures in the range of 30−250 °C were used to obtain the thermal dependence of the cell parameters (Figure 1d). As expected, the unit cell parameters expand nearly linearly with increasing temperature. All cell parameters were transformed to pseudocubic in order to make a comparison between the different polymorphs.

Similar to the K_3AlF_6 polymorph structures described by Abakumov et al.[1] and King et al.,[2] the β-Rb_3ScF_6 structure is derived from the cubic elpasolite structure of γ-Rb_3ScF_6 by rotation of one-fifth of the ScF_6 octahedra with a 45° angle around the c axis. A further 45° rotation of another one-fifth group of ScF_6 octahedra around the a or b axis leads to the α-Rb_3ScF_6 structure. This deformation of the cubic framework leads to changes in the coordination environments for the Rb atoms, while the coordination geometry around the Sc atom does not change and remains octahedral. In comparison with the six-coordinated Rb atoms in the γ form (Figure 3, right),

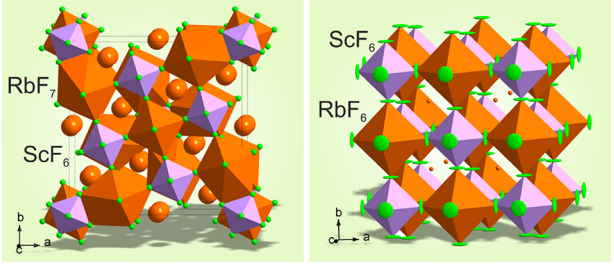

Figure 3. Crystal structures of Rb_3ScF_6: on the left at 187 °C is the β phase and on the right at 250 °C is the γ phase.

four-fifths of these atoms in the β polymorph are in a seven-coordinated pentagonal-bipyramidal environment, while the rest (one-fifth) remain in the octahedral symmetry (Figure 3, left). A further symmetry decay via rotation of another one-fifth group of ScF_6 octahedra results in a further increase in the coordination number (CN) of these Rb atoms in the α phase: three-fifths are seven-coordinated and two-fifths are eight-coordinated (a capped pentagonal bipyramid; Figure 4, right). The geometry of the cubic 12-coordinated Rb sites is also undergoing modifications. Whereas the coordination environment around the Rb1(β) site remains unchanged, Rb2(β) is 11-coordinated by F atoms in the form of an irregular polyhedron. A further distortion of the ideal double perovskite structure in the α polymorph leads to a reduction of the CN of the Rb1(β) site from 12 to 9−11 for the atoms Rb1−Rb7, Rb11, Rb14, and Rb16. Rb10, Rb15, and Rb17 retain a 12-fold coordination.

It should be pointed out that, unlike K_3AlF_6 but like K_3GaF_6,[30] β-Rb_3ScF_6 transforms directly into a cubic γ phase

https://doi.org/10.1021/acs.inorgchem.1c00485
Inorg. Chem. 2021, 60, 6016−6026

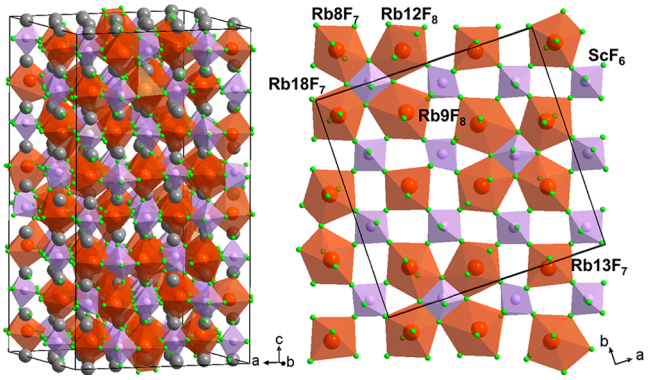

Figure 4. On the left: One unit cell of α-Rb_3ScF_6. Orange (Rb) and violet (Sc) polyhedra form the network, gray is Rb in the cavities, and green is F. On the right: Single layer of Sc and Rb coordination polyhedra viewed down the *c* axis of α-Rb_3ScF_6.

without going through an intermediate γ-K_3AlF_6 with the *Fddd* (No. 70) space group. Our results are partially consistent with the former research work from Turrell et al.[14] in which isolated ScF_6^{3-} octahedra were observed for all polymorphs and the cell parameter for the cubic phase was reported as a = 9.214 Å at 250 °C.

It is worth noting that Rb_3ScF_6 is another new member of a small family but, expanding in recent years, of a double perovskite with NCOT. To the best of our knowledge, this group currently includes (K or Rb)$_3AlF_6$,[1,2,18] Sr_3WO_6,[31] (Ba or Sr)$_3TeO_6$,[32] Rb_2K(Cr or Ga)F_6,[33] K_3GaF_6,[30] (K or Rb)$_3MoO_3F_3$,[34] Rb_3InCl_6,[35] and $Cs_{1.17}In_{0.81}Cl_3$.[36]

Solid-State NMR. From our work on the powder diffraction data, the crystal structure of α-Rb_3ScF_6 contains five Sc sites in octahedral environments with the same multiplicities, along with 18 Rb and 30 F sites. All F atoms are terminal, i.e., nonbridging.

^{45}Sc MAS NMR spectra recorded at 17.6 and 20 T contain three signals (blue line, Figure 5), which are reconstructed by four contributions with relative intensities 1:1:2:1 (Table 2 and Figures 5 and S4). The line with higher integral intensity corresponds to two Sc sites. The ^{45}Sc chemical shift values for six- and seven-coordinated Sc environments range from −32 to 14 ppm and from −67 to −40 ppm, respectively.[12,28] To the best of our knowledge, solid-state NMR data of an eight-coordinated Sc environment were not previously reported in the literature. Therefore, from the Sc NMR results, all Sc sites are six-coordinated. The assignment of the lines to the Sc sites from the integral intensities or the quadrupolar parameters cannot be provided.

Table 2. ^{45}Sc Isotropic Chemical Shifts (δ_{iso}), Quadrupolar Constants (C_Q), Asymmetry Parameters (η_Q), and Integral Intensities (I) Obtained from the Simulation of the ^{45}Sc MAS NMR at 17.6 and 20 T

δ_{iso}, ppm (±0.2 ppm)	C_Q, MHz (±0.1 MHz)	η_Q (±0.1)	I, % (±2%)
19.2	2.3	0.7	21
18.3	3.6	0.8	39
8.1	2.2	0.95	18
6.3	4.2	1	22

Not surprisingly, we observed a decrease in the resolution of the RT ^{45}Sc NMR spectrum while decreasing the MAS rotation frequency from 30 to 6 kHz, but the three ^{45}Sc peaks can still be clearly distinguished (Figure 6).

It should be emphasized that MAS raises the sample temperature due to frictional heating and that the sample temperature without temperature regulation was 31 °C at a spinning frequency of 6 kHz and 56 °C at 30 kHz instead of RT.

The phase transitions in Rb_3ScF_6 are clearly illustrated by the temperature evolution of the ^{45}Sc NMR spectra (Figure 6).

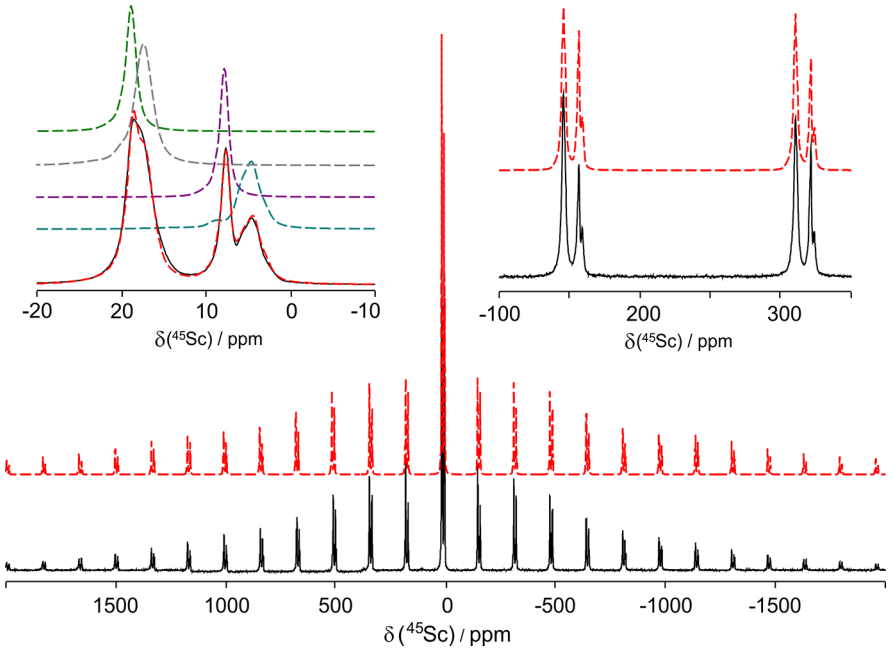

Figure 5. ^{45}Sc MAS NMR experimental (black lines) spectrum of α-Rb_3ScF_6 recorded at 17.6 T and 30 kHz presented with its simulations (dashed red lines). Insets show expanded ^{45}Sc MAS NMR spectra in the region of the central transition (left) and expanded satellite transition sidebands (right). Dashed color lines display the decomposition of the theoretical spectrum in its individual components.

https://doi.org/10.1021/acs.inorgchem.1c00485
Inorg. Chem. 2021, 60, 6016−6026

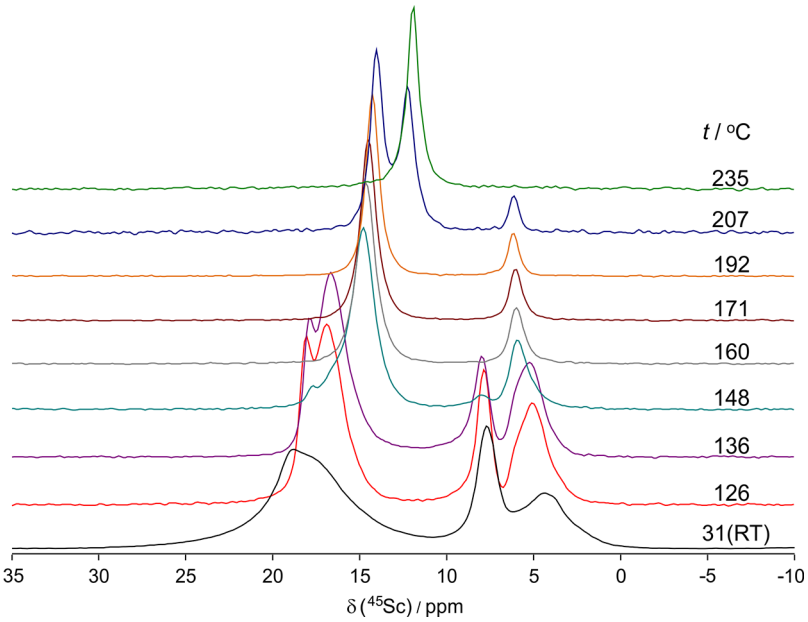

Figure 6. ^{45}Sc NMR spectra of Rb_3ScF_6 acquired at 17.6 T and a MAS frequency of 6 kHz as a function of the temperature.

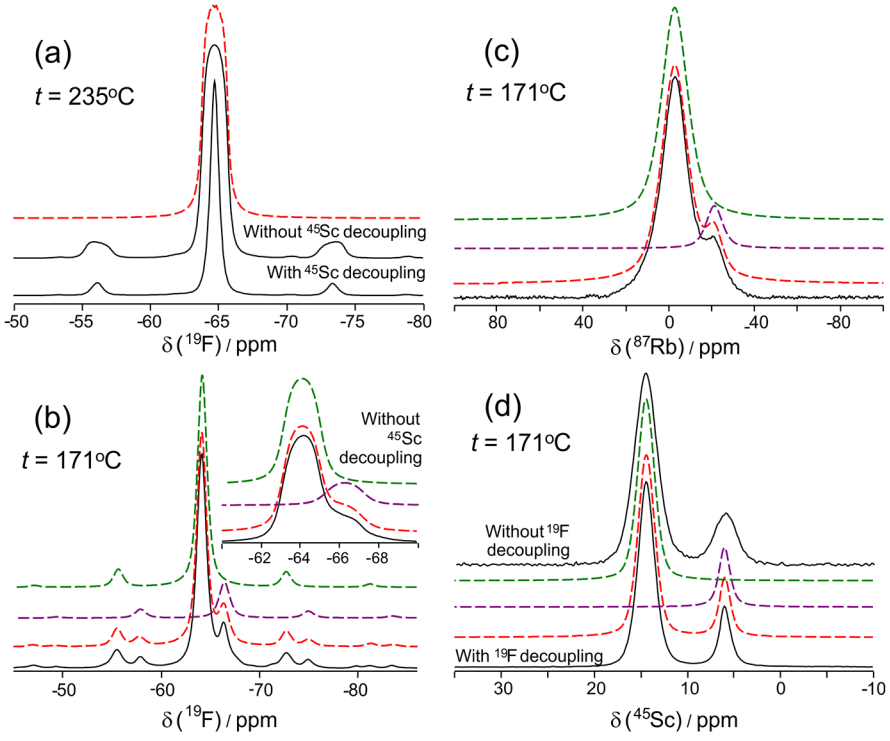

Figure 7. Experimental (black) and simulated (red) ^{19}F (a and b), ^{87}Rb (c), and ^{45}Sc (d) NMR spectra at 17.6 T and a MAS frequency of 6 kHz. The inset in part b shows the ^{19}F spectrum and its simulation without ^{45}Sc decoupling. Colored dashed curves show decomposition of the theoretical spectrum in its individual components.

Upon heating, the ^{45}Sc peaks sharpen notably. When reaching the α-Rb_3ScF_6-to-β-Rb_3ScF_6 phase transition temperature, the ^{45}Sc resonances further narrow and a shift is also observed. At 148 °C, i.e., slightly higher than the α-to-β phase transition temperature, the peak at around 8 ppm has almost disappeared. As stated in the experimental part, the temperature gradient within the rotor affects the spectrum. As a result, at 148 °C, the coexistence of both the α and β phases was found. Above this temperature, because of the fast motion, the spinning sidebands almost disappear. In the range 142−207 °C, the tetragonal β phase exists. The structure of β-Rb_3ScF_6 contains two Sc crystallographic sites with multiplicities of 2:8. The spectra recorded in this temperature range exhibit two narrow lines [full width at half-maximum (fwhm) of 130 ± 20 and 170 ± 20 Hz] with relative intensities of the signals of 1:4. The line shapes were simulated using a mixed Lorentz/Gauss function. The intense resonance at an isotropic chemical shift (δ_{iso}) of 14.4 ppm is assigned to the Sc site with a multiplicity

https://doi.org/10.1021/acs.inorgchem.1c00485
Inorg. Chem. 2021, 60, 6016−6026

of 8 (Sc2) and the small line at δ_{iso} of 5.9 ppm to the Sc site with a multiplicity of 2 (Sc1; Figure 7d). At the phase transition temperature, the coexistence of both polymorphs occurs. Above 207 °C, only a singlet Lorentzian line (δ_{iso} = 11.9 ppm; fwhm = 160 Hz at 235 °C), corresponding to the γ phase, is observed. Thereby, ^{45}Sc MAS NMR observations agree well with the structural models of all polymorphs. The transition temperatures correlate well with the data obtained by DSC.

The ^{19}F NMR spectrum recorded at 20 T and 60 kHz (Figure S5) consists of a broad envelope of signals in the −57 to −70 ppm range. Complete simulation of the spectrum using Lorentzian lines revealed a minimum of eight signals (30 are expected). It was not possible to perform an assignment of the lines to the different F sites.

As in the case of ^{45}Sc NMR, a decrease of the MAS rotation frequency from 30 to 6 kHz induces a decrease in the resolution of the ^{19}F NMR spectrum, and upon heating to 126 °C, the ^{19}F lines sharpen up (Figure S6).

After the α-to-β phase transition, the ^{19}F MAS NMR spectrum of β-Rb_3ScF_6 measured at 171 °C exhibits two peaks (Figure 7b). Accurate simulation of the spectrum, including all spinning-sideband patterns, allowed one to obtain the 1:4 integral intensity ratio for the resonances at −66.4 and −64.1 ppm (fwhm of 910 and 810 Hz), respectively (Table 3). The discrepancy between the expected seven signals and the observed two resonances can be explained in two possible different ways. The first "classic" interpretation is that the line with low intensity corresponds to two F atoms with occupations of 4 and 8, and the second intensive line corresponds to all of the remaining F atoms, i.e., four sites with an occupation of 8 and one site with an occupation of 16. In this case, the chemical shifts of two F atoms for the first peak and five F atoms for the second must be very close. Another possible explanation of the discrepancy is related to the complex dynamics of the system, such as fast hopping of the F atom on each position around one ScF_6 octahedron or, in other terms, to rotational disorder of ScF_6 octahedra. In that case, ^{19}F δ_{iso} appears as the barycenter of the individual δ_{iso} values. The multiplicities of the Sc1:Sc2 sites are 2:8, and the expected integrated intensity ratio agrees well with the experimental value. Previous works showed that this behavior is frequently observed in fluorides.[19,37−39] For example, the γ-K_3AlF_6[2] and β-Rb_3AlF_6[18] polymorphs of the cryolite family contain 11 crystallographic inequivalent F sites, and only four NMR lines can be observed in the experimental spectrum. Another example is the metastable $K_{18}Ta_5Zr_5F_{63}$ compound, in which seven F sites and five signals were detected, corresponding to all five nonequivalent polyhedra.[37] The dynamic of F atoms in γ-K_3AlF_6 and β-Rb_3AlF_6 was more widely studied.[19] It should also be noted that a similar rotational disorder of the (Mo or W)O_4 tetrahedra was observed in the (Ca, Sr, or Ba)MoO_4 scheelite and NaRE[(Mo or W)O_4]$_2$ scheelite-type compounds.[40−42]

To determine the correct explanation, we addressed GIPAW (Gauge Including Projector Augmented Waves) calculations of the NMR parameters. Figure S7 shows the ^{19}F experimental and reconstructed spectra of β-Rb_3ScF_6. As evidenced from this figure, there is a large discrepancy between the two spectra. In order to calculate the ^{19}F chemical shift values according to the second model, we averaged the calculated F positions for each of the polyhedra: Sc2F3F4F5F6F7$_2$ and Sc1F1$_4$F2$_2$. Good overall agreement between the obtained values and the experimental data was observed (Table 3). Thereby, the second assumption is acceptable and coherent with the proposed structural model, and the first assumption is unlikely to take place in practice. Another confirmation of the proposed dynamic model is the absence of a quadrupole line shape in the Sc spectrum. GIPAW calculations lead to large quadrupolar constants of 13.3 and 5.9 MHz for Sc1 and Sc2 sites, respectively. In fact, as indicated above, the ^{45}Sc MAS NMR spectrum revealed two well-defined signals with a Gaussian/Lorentzian line shape because of faster reorientation. It should be mentioned that the calculated chemical shift values fit well with those observed (Table 4).

Table 3. Experimental (Isotropic Chemical Shift δ_{iso} and Integral Intensity I) and Calculated (Isotropic Magnetic Shielding σ_{iso} and Isotropic Chemical Shift $\delta_{calciso}$) ^{19}F NMR Parameters of β-Rb_3ScF_6

F site	σ_{iso}, ppm	$\delta_{calciso}$, ppm	$\langle\delta_{calciso}\rangle$, ppm	δ_{iso}, ppm (±0.1 ppm)	I, % (±1%)
F1	193.61	−71.52	−68.1 (Sc1F1$_4$F2$_2$)	−66.4	20
F2	179.72	−61.38			
F3	184.80	−65.09	−67.8 (Sc2F3F4F5F6F7$_2$)	−64.1	80
F4	193.27	−71.28			
F5	174.05	−57.24			
F6	195.68	−73.03			
F7	191.66	−70.10			

Table 4. ^{45}Sc Isotropic Chemical Shifts (δ_{iso}) and Integral Intensities (I) Obtained from the Simulation of the ^{45}Sc MAS NMR at 17.6 T and Calculated Isotropic Magnetic Shielding σ_{iso} of β- and γ-Rb_3ScF_6

polymorph	atom	δ_{iso}, ppm (±0.2 ppm)	I, % (±1%)	σ_{iso}, ppm	$\delta_{isocalc}$, ppm
β	Sc1	5.9	20	799.07	7.23
	Sc2	14.4	80	788.85	15.73
γ	Sc1	11.90	100	791.06	13.89

In the case of the ^{87}Rb NMR spectrum recorded at RT, a significant signal overlap is observed, resulting from the large number of Rb sites (18) and their quadrupolar broadening (Figure S8). To overcome these limitations, we performed 2D MQMAS NMR experiments.

Because a conventional Z-filtered MQMAS NMR experiment at 17.6 T was unable to provide a sufficient signal-to-noise ratio for signals with a large value of quadrupole constants (even after 4 days of data accumulation), we turned to the RIACT excitation method. The RIACT method is recognized for improving the excitation of sites undergoing large quadrupolar couplings for $I = {}^3/_2$ nuclei, thus improving the sensitivity, at the cost of a more complex line shape arising from nonuniform excitation.[18] Figures 8, S9, and S10 show RIACT and Z-filter MQMAS NMR spectra recorded at 17.6 and 20 T with the same rotor. As expected, the RIACT spectra demonstrate better signal-to-noise ratios. The 2D ^{87}Rb RIACT NMR spectrum recorded at 20 T reveals six resolved peaks with large quadrupole constants ranging between 5.7 and 8.7 MHz and eight lines close to the diagonal slope with a small quadrupole splitting on the order of 2 MHz. The modeling of 1D spectra acquired at two different fields (17.6 and 20 T), while using the NMR parameters obtained from fits of the

https://doi.org/10.1021/acs.inorgchem.1c00485
Inorg. Chem. 2021, 60, 6016−6026

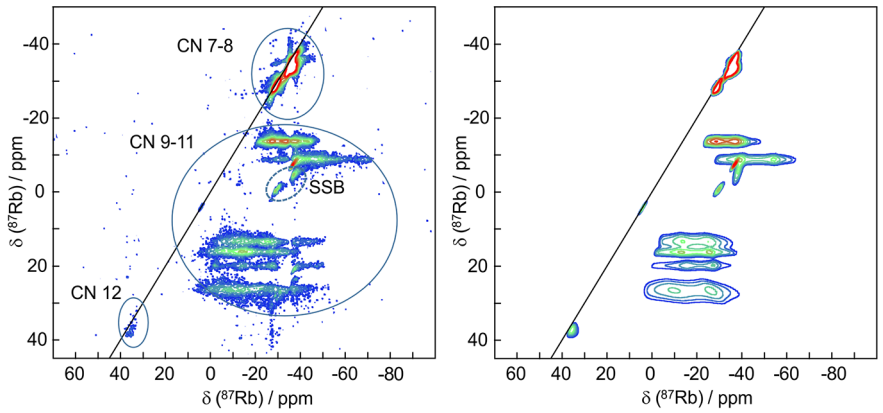

Figure 8. Experimental ^{87}Rb RIACT MQMAS (left) NMR spectrum of Rb_3ScF_6 at 20 T and a spinning rate of 30 kHz and its simulation (right) with the parameters presented in Table 5.

Table 5. ^{87}Rb Isotropic Chemical Shifts (δ_{iso}), Mean Quadrupolar Constants (C_Q), and Relative Intensities Obtained from Simulation of the ^{87}Rb MAS and RIACT MQMAS NMR at 17.6 and 20 T

δ_{iso}, ppm (±0.2 ppm)	C_Q, MHz (±0.4 MHz)	η_Q (±0.2)
−21.9	5.6	0.34
−25.0	7.6	0.66
−29.9	0.95	0.61
−28.8	1.0	0.61
−28.3	1.1	0.61
−35.6	1.0	0.61
−34.3	2.1	0.85
−34.3	1.3	0.41
−0.8	7.6	0.46
1.1	7.3	0.52
2.4	8.1	0.84
7.3	8.3	0.01
4.3	1.5	0.418
36.6	1.8	0.61
45.6	11.8	0.5

RIACT spectra further revealed a missing intensity in the 10−30 ppm chemical shift range. Therefore, we assumed that the 1D spectra contain a supplementary line with a quadrupole constant large enough to remain undetected even when using the RIACT excitation. Figure S8 depicts the simulated 1D spectra with 14 lines obtained from the 2D results and one additional line with C_Q = 11.8 MHz and η_Q = 0.5. It should be pointed out that the strong overlap of the ^{87}Rb resonances makes it impossible to obtain unambiguous values of the integral intensities. While the NMR spectra allow one to identify 15 resolved contributions, the above-described structure of α-Rb_3ScF_6 features 18 independent Rb atomic positions. We propose to ascribe the group of high-field peak Rb sites with CNs of 7 and 8; the two sets of lines with the largest C_Q values are ascribed to the Rb sites with CNs of 9−11; the two small 2D spots close to the diagonal slope can be assigned to a Rb site with CN 12. Thus, even though it remains impossible to perform an accurate spectral assignment of the ^{87}Rb NMR resonances with the crystallographic sites, our results allow one to estimate the values of the ^{87}Rb NMR parameters and to propose the line assignment.

The temperature dependence of the ^{87}Rb NMR spectra exhibits variations similar to those in the cases of variable-temperature ^{19}F and ^{45}Sc NMR measurements (Figure S11). At 148 °C, the spectrum contains a set of signals corresponding to the α and β polymorphs. The ^{87}Rb MAS NMR spectrum of β-Rb_3ScF_6 at 171 °C presents two resonances at −21.7 and −2.6 ppm with relative intensities and line widths of 13%/2100 Hz and 87%/3500 Hz, respectively. According to the site multiplicities, line 1 can be assigned to the Rb1 (4d) site and line 2 to the sum of all other sites (16i, 2b, and 8h), respectively. The ^{19}F and ^{87}Rb NMR spectra recorded at 207 °C clearly indicate the phase transition from β-Rb_3ScF_6 to γ-Rb_3ScF_6. Each of the rubidium and fluorine NMR spectra was reconstructed using a single Lorentz line with chemical shifts at 2.2 and −64.7 ppm at 235 °C (fwhm = 156 and 520 Hz), respectively. The resulting disagreement with the presence of two Rb sites of 4b and 8c multiplicity in the structure can be explained by the presence of the two Rb sites of γ-Rb_3ScF_6, which are involved in the chemical exchange. It should be noted that the same exchange process was observed for β-Rb_3AlF_6.[19] A good agreement between the calculated ^{19}F and ^{45}Sc shielding constants of γ-Rb_3ScF_6 and the experimental chemical shifts was obtained (Tables 3 and 4). The temperature dependence of all NMR spectra demonstrated the overall reversibility of the spectral changes.

King et al.[2] observed the dynamic rotations of AlF_6 octahedra in δ-K_3AlF_6, and they proposed that "such rotations could be occurring in some of the lower temperature phases as well." We also view this dynamic as a fast hopping mechanism of the F on each position around one AlF_6 octahedron.[19] This conjecture was confirmed by the investigation of isostructural γ-K_3AlF_6 and α-Rb_3AlF_6. In this study, we confirm this assumption for β-Rb_3ScF_6. On the basis of these findings, we revised the ^{19}F MAS NMR spectrum of β-K_3AlF_6, which is isostructural with β-Rb_3ScF_6. It contains an asymmetrically broadened peak, which is reconstructed with two individual contributions. Unfortunately, the lack of resolution of the spectrum does not allow one to correctly and unequivocally measure the integrated intensity. The resulting 1:5 ratio is slightly higher than the expected one (1:4). Therefore, it appears that rotation of the AlF_6 octahedra is very likely to take place in β-K_3AlF_6. It is worth noting that no such rotation was observed in the α polymorphs of K_3AlF_6 and Rb_3ScF_6. If there was a fast hopping mechanism of the F on each position around one AlF_6 octahedron, only five lines would be observed

https://doi.org/10.1021/acs.inorgchem.1c00485
Inorg. Chem. 2021, 60, 6016−6026

in the fluorine NMR spectrum, in agreement with the number of crystallographically nonequivalent Al/Sc sites.

The ^{19}F line shapes of both the β-Rb_3ScF_6 and γ-Rb_3ScF_6 spectra recorded without Sc decoupling can be ascribed as nonresolved multiplets (Figure 7a,b). From the fitted spectrum, the coupling constant values are $^1J(^{45}Sc,^{19}F)$ 164 and 167 Hz for the β phase and 160 Hz for the γ phase. These values are in good agreement with the previous results obtained for fluoroscandates.[28,43]

CONCLUSIONS

In this work, the interplay between X-ray and neutron powder diffraction, solid-state NMR, SAED, and theoretical calculations is exploited in order to achieve an accurate description of the structure of the three α-, β-, and γ-Rb_3ScF_6 polymorphs. The structures, two tetragonal and one cubic forms, were determined from X-ray and neutron powder diffraction structural analysis based on isostructural K_3AlF_6 models, and these were further confirmed by solid-state NMR and SAED methods. The structural correlation between the three polymorphs was also discussed. Two new examples of NCOT are reported. HT MAS NMR appears as a powerful method that enables in situ monitoring of the local dynamics of ScF_6 octahedra and phase transitions. A good agreement was achieved for the observed and calculated NMR parameters. We expect this work to stimulate future opportunities in the synthesis and investigation of Mn^{4+} or lanthanide-doped Rb_3ScF_6 with interesting optical properties.

ASSOCIATED CONTENT

Supporting Information

The Supporting Information is available free of charge at https://pubs.acs.org/doi/10.1021/acs.inorgchem.1c00485.

Tables of atomic coordinates and ADPs and of bond distances, $R^2(U)$ and $\delta_{iso}(\sigma_{iso})$, DSC, neutron diffraction data, ^{45}Sc, ^{19}F, and ^{87}Rb MAS NMR, ^{87}Rb Z-filter, and RIACT MQMAS (PDF)

Accession Codes

CCDC 2027066,2027067, and 2062818 contain the supplementary crystallographic data for this paper. These data can be obtained free of charge via www.ccdc.cam.ac.uk/data_request/cif, or by emailing data_request@ccdc.cam.ac.uk, or by contacting The Cambridge Crystallographic Data Centre, 12 Union Road, Cambridge CB2 1EZ, UK; fax: +44 1223 336033.

AUTHOR INFORMATION

Corresponding Author

Aydar Rakhmatullin − *Conditions Extrêmes et Matériaux: Haute Température et Irradiation, CEMHTI, UPR 3079, CNRS, Université Orléans, Orléans 45071, France;* orcid.org/0000-0002-7328-5081; Phone: +33 238 25 55 12; Email: rakhmat@cnrs-orleans.fr; Fax: +33 238 63 81 03

Authors

Maxim S. Molokeev − *Laboratory of Crystal Physics, Kirensky Institute of Physics, Federal Research Center Krasnoyarsk Science Center of the Siberian Branch of the Russian Academy of Sciences, Krasnoyarsk 660036, Russia; Siberian Federal University, Krasnoyarsk 660041, Russia;* orcid.org/0000-0002-8297-0945

Graham King − *Material and Chemical Sciences, Canadian Light Source, Saskatoon, Saskatchewan S7N 2V3, Canada;* orcid.org/0000-0003-1886-7254

Ilya B. Polovov − *Department of Rare Metals and Nanomaterials, Institute of Physics and Technology, Ural Federal University, Ekaterinburg 620002, Russia*

Konstantin V. Maksimtsev − *Department of Rare Metals and Nanomaterials, Institute of Physics and Technology, Ural Federal University, Ekaterinburg 620002, Russia*

Erwan Chesneau − *Conditions Extrêmes et Matériaux: Haute Température et Irradiation, CEMHTI, UPR 3079, CNRS, Université Orléans, Orléans 45071, France*

Emmanuelle Suard − *Institut Laue-Langevin, Grenoble 9 F-38042, France;* orcid.org/0000-0001-5966-5929

Rinat Bakirov − *Department of Technology of Mechanical Engineering and Instrument Making, Votkinsk Branch of Kalashnikov Izhevsk State Technical University, Votkinsk 427000, Russia*

František Šimko − *Institute of Inorganic Chemistry and Centre of Excellence for Advanced Materials Application, CEMEA, Slovak Academy of Sciences, Bratislava 84536, Slovakia;* orcid.org/0000-0003-2390-1349

Catherine Bessada − *Conditions Extrêmes et Matériaux: Haute Température et Irradiation, CEMHTI, UPR 3079, CNRS, Université Orléans, Orléans 45071, France*

Mathieu Allix − *Conditions Extrêmes et Matériaux: Haute Température et Irradiation, CEMHTI, UPR 3079, CNRS, Université Orléans, Orléans 45071, France;* orcid.org/0000-0001-9317-1316

Complete contact information is available at: https://pubs.acs.org/10.1021/acs.inorgchem.1c00485

Author Contributions

A.R. conceptualized and planned the project. F.S. performed the DSC experiments. M.S.M., G.K., and M.A. performed structural analysis. M.A. performed HT X-ray diffraction experiments. E.S. performed neutron experiments. A.R. conducted all of the NMR experiments with assistance from E.C. and C.B. I.B.P., R.B., and K.V.M. performed the synthesis experiments. A.R. carried out the CASTEP calculations. The manuscript was written with contribution from all coauthors.

Notes

The authors declare no competing financial interest.

ACKNOWLEDGMENTS

For DFT calculations, we thank the "Centre de Calcul Scientifique en region Centre" (Orléans, France). We acknowledge the Interface, Confinement, Materials and Nanostructures (Orléans, France) for access to their transmission electron microscope. Financial support from the IR-RMN-THC Fr3050 CNRS for conducting the research is gratefully acknowledged. This study was also financially supported by VEGA-2/0060/18 and ITMS project (code 313021T081, Research & Innovation Operational Programme funded by the ERDF). We thank also Dr. F. Vivet, Dr. F. Fayon, and Dr. D. Massiot for useful discussions.

REFERENCES

(1) Abakumov, A. M.; King, G.; Laurinavichute, V. K.; Rozova, M. G.; Woodward, P. M.; Antipov, E. V. The Crystal Structure of α-K_3AlF_6: Elpasolites and Double Perovskites with Broken Corner-

Sharing Connectivity of the Octahedral Framework. *Inorg. Chem.* **2009**, *48* (19), 9336−9344.
(2) King, G.; Abakumov, A. M.; Woodward, P. M.; Llobet, A.; Tsirlin, A. A.; Batuk, D.; Antipov, E. V. The High-Temperature Polymorphs of K_3AlF_6. *Inorg. Chem.* **2011**, *50* (16), 7792−7801.
(3) Ai, Y.; Tu, D.; Zheng, W.; Liu, Y.; Kong, J.; Hu, P.; Chen, Z.; Huang, M.; Chen, X. Lanthanide-doped $NaScF_4$ nanoprobes: crystal structure, optical spectroscopy and biodetection. *Nanoscale* **2013**, *5* (14), 6430−6438.
(4) Yu, B.; Hao, E.; Fang, S.; Liu, Z.; Wang, Y.; Lv, Z.; Li, N.; Zhang, X.; Shi, L.; Du, Y. Controlled synthesis of high quality scandium-based nanocrystals as promising recyclable catalysts for silylcyanation reaction. *Nanoscale* **2017**, *9* (31), 10987−10991.
(5) Xiong, J.; Yu, J.; Zhang, Y.; Xia, W.; Hu, S.; Zhang, Y.; Yang, J. One-step surfactant-free synthesis of KSc_2F_7 microcrystals: controllable phases, rich morphologies and multicolor down conversion luminescence properties. *CrystEngComm* **2018**, *20* (28), 3978−3986.
(6) Zhang, L.; Zhao, S.; Liang, Z.; Zhang, J.; Zhu, W.; Liu, P.; Sun, H. The colour tuning of upconversion emission from green to red in $NaScF_4$:Yb^{3+}/Er^{3+} nanocrystals by adjusting the reaction time. *J. Alloys Compd.* **2017**, *699*, 1−6.
(7) Tyagi, A. K.; Köhler, J.; Balog, P.; Weber, J. Syntheses and structures of Li_3ScF_6 and high pressure $LiScF_4$, luminescence properties of $LiScF_4$, a new phase in the system LiF-ScF_3. *J. Solid State Chem.* **2005**, *178* (9), 2620−2625.
(8) Chen, D.; Peng, Y.; Li, X.; Zhong, J.; Huang, H.; Chen, J. Simultaneous Tailoring of Dual-Phase Fluoride Precipitation and Dopant Distribution in Glass to Control Upconverting Luminescence. *ACS Appl. Mater. Interfaces* **2019**, *11* (33), 30053−30064.
(9) Ming, H.; Liu, S.; Liu, L.; Peng, J.; Fu, J.; Du, F.; Ye, X. Highly Regular, Uniform K_3ScF_6:Mn^{4+} Phosphors: Facile Synthesis, Microstructures, Photoluminescence Properties, and Application in Light-Emitting Diode Devices. *ACS Appl. Mater. Interfaces* **2018**, *10* (23), 19783−19795.
(10) Song, E.; Wang, J.; Shi, J.; Deng, T.; Ye, S.; Peng, M.; Wang, J.; Wondraczek, L.; Zhang, Q. Highly Efficient and Thermally Stable K_3AlF_6:Mn^{4+} as a Red Phosphor for Ultra-High-Performance Warm White Light-Emitting Diodes. *ACS Appl. Mater. Interfaces* **2017**, *9* (10), 8805−8812.
(11) Krylov, A. S.; Molokeev, M. S.; Misyul, S. V.; Krylova, S. N.; Oreshonkov, A. S.; Ivanenko, A. A.; Zykova, V. A.; Ivanov, Y. N.; Sukhovsky, A. A.; Voronov, V. N.; Safonov, I. N.; Vtyurin, A. N. Crystal structure and phase transitions of a layered perovskite-like $CsScF_4$ crystal. *CrystEngComm* **2016**, *18* (43), 8472−8486.
(12) Rakhmatullin, A.; Allix, M.; Polovov, I. B.; Maltsev, D.; Chukin, A. V.; Bakirov, R.; Bessada, C. Combining solid state NMR, powder X-ray diffraction, and DFT calculations for $CsSc_3F_{10}$ structure determination. *J. Alloys Compd.* **2019**, *787*, 1349−1355.
(13) Yin, Y. New Solid-State Fluorides: Synthesis, Crystal Chemistry, and Optical Properties. Ph.D. Thesis, Oregon State University, Corvallis, OR, 1993.
(14) Turrell, S.; Hafsi, S.; Conflant, P.; Barbier, P.; Drache, M.; Champarnaud-Mesjard, J. C. Vibrational spectra, phase transitions and force-fields in crystalline scandium hexafluorides. *J. Mol. Struct.* **1988**, *174*, 449−454.
(15) *TOPAS 4.2 User's Manual. General profile and structure analysis software for powder diffraction data*; Bruker AXS: Karlsruhe, Germany, 2009.
(16) Petříček, V.; Dušek, M.; Palatinus, L. Crystallographic Computing System JANA2006: General features. *Z. Kristallogr. - Cryst. Mater.* **2014**, *229*, 345−352.
(17) Massiot, D. Sensitivity and Lineshape Improvements of MQ-MAS by Rotor-Synchronized Data Acquisition. *J. Magn. Reson., Ser. A* **1996**, *122* (2), 240−244.
(18) Wu, G.; Rovnyak, D.; Griffin, R. G. Quantitative Multiple-Quantum Magic-Angle-Spinning NMR Spectroscopy of Quadrupolar Nuclei in Solids. *J. Am. Chem. Soc.* **1996**, *118* (39), 9326−9332.
(19) Rakhmatullin, A.; Šimko, F.; Véron, E.; Allix, M.; Martineau-Corcos, C.; Fitch, A.; Fayon, F.; Shakhovoy, R. A.; Okhotnikov, K.; Sarou-Kanian, V.; Korenko, M.; Netriová, Z.; Polovov, I. B.; Bessada, C. X-ray Diffraction, NMR Studies, and DFT Calculations of the Room and High Temperature Structures of Rubidium Cryolite, Rb_3AlF_6. *Inorg. Chem.* **2020**, *59* (9), 6308−6318.
(20) Angeli, F.; Charpentier, T.; De Ligny, D.; Cailleteau, C. Boron Speciation in Soda-Lime Borosilicate Glasses Containing Zirconium. *J. Am. Ceram. Soc.* **2010**, *93* (9), 2693−2704.
(21) Weingarth, M.; Bodenhausen, G.; Tekely, P. Probing the quenching of rotary resonance by PISSARRO decoupling. *Chem. Phys. Lett.* **2011**, *502* (4−6), 259−265.
(22) Massiot, D.; Fayon, F.; Capron, M.; King, I.; Le Calvé, S.; Alonso, B.; Durand, J. O.; Bujoli, B.; Gan, Z.; Hoatson, G. Modelling one and two-dimensional solid-state NMR spectra. *Magn. Reson. Chem.* **2002**, *40* (1), 70−76.
(23) Charpentier, T.; Fermon, C.; Virlet, J. Numerical and theoretical analysis of multiquantum magic-angle spinning experiments. *J. Chem. Phys.* **1998**, *109* (8), 3116−3130.
(24) Perdew, J. P.; Burke, K.; Ernzerhof, M. Generalized Gradient Approximation Made Simple. *Phys. Rev. Lett.* **1996**, *77* (18), 3865−3868.
(25) Profeta, M.; Benoit, M.; Mauri, F.; Pickard, C. J. First-Principles Calculation of the ^{17}O NMR Parameters in Ca Oxide and Ca Aluminosilicates: the Partially Covalent Nature of the Ca-O Bond, a Challenge for Density Functional Theory. *J. Am. Chem. Soc.* **2004**, *126* (39), 12628−12635.
(26) Sadoc, A.; Body, M.; Legein, C.; Biswal, M.; Fayon, F.; Rocquefelte, X.; Boucher, F. NMR parameters in alkali, alkaline earth and rare earth fluorides from first principle calculations. *Phys. Chem. Chem. Phys.* **2011**, *13* (41), 18539−18550.
(27) Clark, S. J.; Segall, M. D.; Pickard, C. J.; Hasnip, P. J.; Probert, M. I. J.; Refson, K.; Payne, M. C. First principles methods using CASTEP. *Z. Kristallogr. - Cryst. Mater.* **2005**, *220* (5/6), 567−570.
(28) Rakhmatullin, A.; Polovov, I. B.; Maltsev, D.; Allix, M.; Volkovich, V.; Chukin, A. V.; Boča, M.; Bessada, C. Combined Approach for the Structural Characterization of Alkali Fluoroscandates: Solid-State NMR, Powder X-ray Diffraction, and Density Functional Theory Calculations. *Inorg. Chem.* **2018**, *57* (3), 1184−1195.
(29) Abakumov, A. M.; Rossell, M. D.; Alekseeva, A. M.; Vassiliev, S. Y.; Mudrezova, S. N.; Van Tendeloo, G.; Antipov, E. V. Phase transitions in K_3AlF_6. *J. Solid State Chem.* **2006**, *179* (2), 421−428.
(30) King, G. New examples of non-cooperative octahedral tilting in a double perovskite: phase transitions in K_3GaF_6. *Acta Crystallogr., Sect. B: Struct. Sci., Cryst. Eng. Mater.* **2020**, *76* (5), 789.
(31) King, G.; Abakumov, A. M.; Hadermann, J.; Alekseeva, A. M.; Rozova, M. G.; Perkisas, T.; Woodward, P. M.; Van Tendeloo, G.; Antipov, E. V. Crystal Structure and Phase Transitions in Sr_3WO_6. *Inorg. Chem.* **2010**, *49* (13), 6058−6065.
(32) Stöger, B.; Weil, M.; Zobetz, E. Sr_3TeO_6 and Ba_3TeO_6: double perovskites with pronounced superstructures. *Z. Kristallogr. - Crystalline Materials* **2010**, *225* (4), 125.
(33) Javier Zúñiga, F.; Tressaud, A.; Darriet, J. The low-temperature form of Rb_2KCrF_6 and Rb_2KGaF_6: The first example of an elpasolite-derived structure with pentagonal bipyramid in the B-sublattice. *J. Solid State Chem.* **2006**, *179* (12), 3607−3614.
(34) Fry, A. M.; Woodward, P. M. Structures of α-$K_3MoO_3F_3$ and α-$Rb_3MoO_3F_3$: Ferroelectricity from Anion Ordering and Noncooperative Octahedral Tilting. *Cryst. Growth Des.* **2013**, *13* (12), 5404−5410.
(35) Majher, J. D.; Gray, M. B.; Liu, T.; Holzapfel, N. P.; Woodward, P. M. Rb_3InCl_6: A Monoclinic Double Perovskite Derivative with Bright Sb^{3+}-Activated Photoluminescence. *Inorg. Chem.* **2020**, *59*, 14478.
(36) Tan, X.; Stephens, P. W.; Hendrickx, M.; Hadermann, J.; Segre, C. U.; Croft, M.; Kang, C.-J.; Deng, Z.; Lapidus, S. H.; Kim, S. W.; Jin, C.; Kotliar, G.; Greenblatt, M. Tetragonal $Cs_{1.17}In_{0.81}Cl_3$: A Charge-Ordered Indium Halide Perovskite Derivative. *Chem. Mater.* **2019**, *31* (6), 1981−1989.

https://doi.org/10.1021/acs.inorgchem.1c00485
Inorg. Chem. 2021, 60, 6016−6026

(37) Boča, M.; Molokeev, M. S.; Rakhmatullin, A.; Kubíková, B.; Netriová, Z. The structure of the metastable $K_{18}Ta_5Zr_5F_{63}$ phase. *New J. Chem.* **2020**, *44* (22), 9264−9270.
(38) Smrčok, L.; Le Bail, A.; Boča, M.; Rakhmatullin, A. Polymorphism of K_2ZrF_6. *Cryst. Growth Des.* **2020**, *20* (6), 3867−3881.
(39) Boča, M.; Rakhmatullin, A.; Mlynáriková, J.; Hadzimová, E.; Vasková, Z.; Mičušík, M. Differences in XPS and solid state NMR spectral data and thermo-chemical properties of iso-structural compounds in the series $KTaF_6$, K_2TaF_7 and K_3TaF_8 and $KNbF_6$, K_2NbF_7 and K_3NbF_8. *Dalton Trans.* **2015**, *44* (39), 17106−17117.
(40) Rabuffetti, F. A.; Culver, S. P.; Suescun, L.; Brutchey, R. L. Structural Disorder in $AMoO_4$ (A = Ca, Sr, Ba) Scheelite Nanocrystals. *Inorg. Chem.* **2014**, *53* (2), 1056−1061.
(41) Culver, S. P.; Brutchey, R. L. Thermally activated rotational disorder in $CaMoO_4$ nanocrystals. *CrystEngComm* **2016**, *18* (24), 4485−4488.
(42) Amarasinghe, D. K.; Perera, S. S.; Rabuffetti, F. A. Rotational Disorder in Scheelite-Type $NaRE(MO_4)_2$ (RE = Rare-Earth, Y; M = Mo, W). *Cryst. Growth Des.* **2020**, *20* (5), 3442−3448.
(43) Pfadenhauer, E. H.; McCain, D. C. Nuclear magnetic resonance of fluoroscandate anion, ScF_6^{3-}, in aqueous solution. *J. Phys. Chem.* **1970**, *74* (17), 3291−3293.

https://doi.org/10.1021/acs.inorgchem.1c00485
Inorg. Chem. 2021, 60, 6016−6026